AFRL-AFOSR-VA-TR-2019-0185

Superconducting THz emitters and receivers in YBCO utilizing focused helium beam nanolithography

DOUGLAS PAULSON
Tristan Technologies, Inc.

07/15/2019
Final Report

Air Force Research Laboratory
AF Office Of Scientific Research (AFOSR)/ RTA1
Arlington, Virginia 22203
Air Force Materiel Command

REPORT DOCUMENTATION PAGE

Form Approved
OMB No. 0704-0188

1. REPORT DATE *(DD-MM-YYYY)*	**2. REPORT TYPE**	**3. DATES COVERED** *(From - To)*
03-07-2019	Phase I Final Technical Report	Sep/2018 – Jun/2019

4. TITLE AND SUBTITLE

Superconducting THz emitters and receivers in YBCO utilizing focused helium beam nanolithography

5a. CONTRACT NUMBER
FA9550-18-P-0022

5b. GRANT NUMBER

5c. PROGRAM ELEMENT NUMBER

6. AUTHOR(S)

Dr. Douglas Paulson (Tristan Tech), Kevin Pratt (Tristan Tech), Dr. Shane Cybart (UCR), Dr. Ethan Cho (UCR/SQUIDWorks), Anthony Cortez (UCR)

5d. PROJECT NUMBER

5e. TASK NUMBER

5f. WORK UNIT NUMBER

7. PERFORMING ORGANIZATION NAME(S) AND ADDRESS(ES)

Tristan Technologies Inc; 6191 Cornerstone Ct. E., ste 107; San Diego, CA 92121
University of California at Riverside; 900 University Ave.; Riverside, CA 92521

8. PERFORMING ORGANIZATION REPORT NUMBER

9. SPONSORING / MONITORING AGENCY NAME(S) AND ADDRESS(ES)
Air Force Office of Scientific Research
875 North Randolph Street, room 3112
Arlington, VA 22203-1954

10. SPONSOR/MONITOR'S ACRONYM(S)
AFOSR

11. SPONSOR/MONITOR'S REPORT NUMBER(S)
FA9550-18-P-0022-0001AD

12. DISTRIBUTION / AVAILABILITY STATEMENT

Distribution A – Approved for public release

13. SUPPLEMENTARY NOTES

14. ABSTRACT

Report developed under SBIR contract for topic AF181-004. There exists an under-utilized portion of the electromagnetic spectrum, located between the microwave and infrared wavelengths, known as terahertz radiation. In this Phase I effort, we developed THz transmitters and receivers by using Helium ion beam nano-lithography to fabricate Josephson junction arrays in YBCO, and evaluated their effectiveness at generating and detecting THz radiation. These transmitter and receiver devices were then tested in tandem with the goal of using the receiver to detect power radiated from the emitter at THz frequencies. Furthermore, we have developed a cryopackaging solution for a Phase II prototype THz spectrometer employing these HTS THz transmitters and receivers to interrogate the transmission, reflection, and absorption spectra of a sample-under-test.

15. SUBJECT TERMS
Superconducting, quantum, Terahertz, spectroscopy, nano-lithography, cryogenic, Josephson junction

16. SECURITY CLASSIFICATION OF:			**17. LIMITATION OF ABSTRACT**	**18. NUMBER OF PAGES**	**19a. NAME OF RESPONSIBLE PERSON**
					Kevin Pratt
a. REPORT	**b. ABSTRACT**	**c. THIS PAGE**	UU	19	**19b. TELEPHONE NUMBER** *(include area code)*
U	U	U			(858) 550 – 2700 x104

Standard Form 298 (Rev. 8-98)
Prescribed by ANSI Std. Z39.18

TABLE OF CONTENTS

TABLE OF FIGURES

1.0 IDENTIFICATION OF THE OPPORTUNITY

There exists an under-utilized portion of the electromagnetic spectrum, located between the microwave and infrared wavelengths, in the sub-millimeter band. This region, known as terahertz (THz) radiation, has historically been problematic to access, with frequencies too high for microwave technology generators and detection techniques, and too low for optical methods. This unsuitability of mature technologies has led this frequency regime to be coined the "THz Gap".

Recently, technologies for generating and detecting terahertz radiation have advanced rapidly with the development of Quantum Cascade Lasers (QCL), Free Electron Lasers (FEL), Backward Wave Oscillators (BWO), and sub-picosecond optical excitation of photoconductive devices, to name a few. Potential applications for this under-served frequency band include spectroscopy, imaging, and extreme bandwidth wireless communications. Many molecules exhibit unique absorption spectra in the THz regime, allowing identification of unknown materials (e.g. explosives or illicit drugs) by their spectral "fingerprint" in the THz band. Many organic or synthetic materials of non-polar, non-metallic construction are transparent in the THz band, enabling the remote detection of objects such as concealed firearms. Owing to the high frequency of terahertz signals, short-range wireless networks employing multi-THz carrier frequencies could achieve orders of magnitude increases in data transmission rates.

There have been numerous demonstrations [1-11] of THz electronics using low-temperature superconductivity (LTS) Josephson junctions that provide precise frequency control and on-chip detection via the alternating current (AC) Josephson effect. These devices are accurate to the quantum level and are based on the same physics as the precision voltage standards used by the National Institute for Standards and Technology (NIST) to define the volt. In this prior work, studies of the oscillator line width and similarly related fundamental aspects of Josephson oscillators were established. In particular, early researchers in this area investigated the usage of arrays of coupled junctions to increase the power from single junction devices to ~1μW. It was found that by phase locking N individual oscillators together, power levels could be increased by $\sim N^2$. Several different configurations were demonstrated, including series- and series-parallel arrays.

Unfortunately, the mature technology of Niobium Josephson junction fabrication imposes an upper frequency cutoff of about 0.75 THz, a fundamental limit defined by the superconducting energy gap, Δ, of about 1.5 meV in niobium. The Josephson constant, F_J = 484 THz/V, is a direct result of calculation of the AC Josephson equation. Due to a combination of the low operating temperature (4K) and upper frequency limitations, these types of THz electronics did not transition out of the research laboratory into widespread use.

In 1987, the discovery of High Temperature Superconductivity (HTS) in ceramic materials at temperatures around 90 Kelvin [12] sparked a surge of research in the development of HTS electronics, motivated by the prospects of electronics operating in low-cost liquid nitrogen (77K) as opposed to liquid helium (4K). HTS materials can have energy gaps greater than 40 meV which may allow for frequencies above 10 THz and provide a solution that can cover the entire 1.0 – 10 THz band. There have been numerous demonstrations exhibiting the capabilities of HTS THz electronics employing intrinsic Josephson junctions (IJJ) in $Bi_2Sr_2CaCu_2O_{8+\delta}$ (BSCCO) layers cleaved from single crystals [13-14]. While useful for demonstrations, this method of fabrication is not practical for manufacture of electronics as it is not uniform or reproducible.

More reliable fabrication methods of HTS Josephson junctions (JJ) have been mostly unsuccessful because, historically, they all have metallic diffusive Josephson barriers and small figures of merit ($I_C R_N$) that preclude use at THz frequencies. Recently, the Cybart group at University of California Riverside (UCR) has demonstrated a new, scalable, nano-manufacturing method of HTS devices [15] that has the

potential to deliver large numbers of uniform Josephson junctions while at the same time reducing the costs by orders of magnitude. This method of fabrication of HTS junctions demonstrated by the Cybart group utilizes a focused Helium ion beam to directly write junctions into commercially grown HTS thin films. Unlike prior art manufactured HTS junctions, these junctions exhibit insulating barriers like the intrinsic stack junctions used in BSCCO demonstrations. Furthermore they exhibit large energy gaps of up to 32mV. This new type of junction opens up the direct write manufacture of THz devices in a controlled and manufacturable way.

In this Phase I effort, we proposed to develop THz transmitters and receivers by using this direct-write approach to fabricate Josephson junction arrays in $YBa_2Cu_3O_7$ (YBCO), and evaluate their effectiveness at generating and detecting THz radiation.

2.0 BACKGROUND AND METHODS

2.1 Overview of Josephson Junctions

Josephson junctions comprise the building blocks of superconducting electronics, analogous to transistors in semiconductor devices. A junction consists of two superconducting electrodes separated by an insulating or normal metal layer (**Fig.1(a)**). In the direct-current (DC) Josephson effect [16], superconducting electron pairs can tunnel from one side of the junction to the other, forming a current proportional to the phase difference, θ, of the superconducting order parameter, $\Psi=\psi e^{i\theta}$, where ψ is the superconducting electron pair amplitude, in the absence of a voltage potential difference. The superconducting tunnel current is described by the first Josephson equation, $I = I_C \sin \varphi$, where φ is the phase difference between the two electrodes $\varphi=(\theta_1-\theta_2)$, and I_C is the maximum (critical) super-current of the junction.

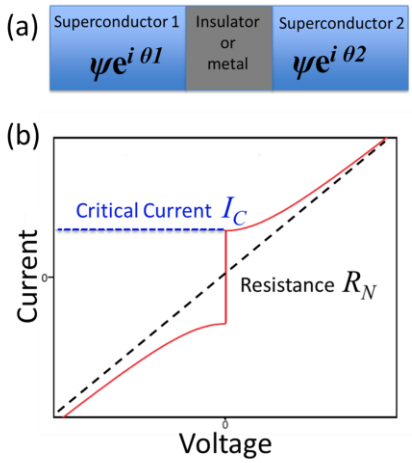

Fig.1: (a) Schematic representation of a Josepshon junction. (b) Current voltage characteristic of a typical Josepshon junction used for electronics, depicting I_C and R_N.

Electrically, a typical current-biased Josephson junction has a non-linear current-voltage characteristic (*I-V*) like that shown in Fig.1(b). The critical current, I_C, appears as a spike at zero voltage. For currents higher than I_C, a voltage appears across the junction and has a resistance, R_N, which approaches Ohm's law at high voltage [17, 18]. The critical voltage, or product of I_C and R_N, is a very important figure of merit for Josephson junctions. I_C is a measure of the coupling energy between the two electrodes and scales exponentially with distance at the sub-10 nanometer scale [18]. R_N is a measure of the barrier strength which is highest for strong insulator barriers.

The second Josephson equation,

$d\varphi/dt = (2\pi*2e/h)*V$,

also gives rise to interesting quantum mechanical effects, namely that when the voltage across a junction is held at a fixed DC value, the phase difference between the two superconducting electrodes increases at a fixed time rate of change. This constantly changing phase generates a *very* high frequency AC current across the junction, with a frequency defined by the Josephson constant, F_J = 484 THz/V, and is known as the AC Josephson effect. Another interesting phenomenon, the inverse AC Josephson effect, can be observed by bathing the junction in (typically) microwave radiation. When the voltage applied across the junction is equal to an integer multiple of the voltage inferred by

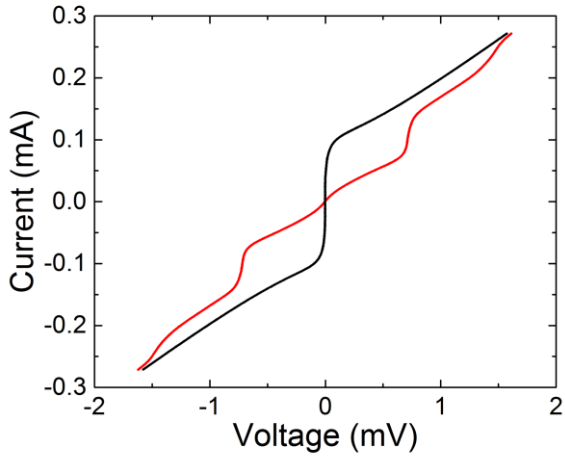

Fig.2: I-V of YBCO, Josephson junction array containing 20 junctions. With (red) and without (black) applied 17.6 GHz microwave radiation. A giant Shapiro step is observed at 20hf/2e= 0.727 mV.

the frequency of the applied microwaves, a spike in the DC current through the junction is observed, known as Shapiro steps (see **Fig.2**). We aim to employ the AC Josephson effect to generate AC currents in junction arrays, which then generate electromagnetic radiation at the induced frequency. The inverse AC Josephson effect, likewise, can be employed as a detector methodology, where *I-V* sweeps of the detector junction effectively downconvert detected THz signals to quasi-DC when the Josephson frequency of the voltage applied across the detector junction is equal to the frequency of the incident THz radiation.

2.2 Focused Helium Ion Beam Nano-Junctions

In the last three decades, there has been considerable effort in developing a HTS Josephson junction manufacturing technology capable of producing large numbers of junctions with uniform and controllable $I_C R_N$ [19]. This is especially challenging in HTS compared with LTS because the superconducting coherence length (ξ) is much shorter and highly anisotropic [20], typically only 2 nm in the *ab*-plane and 0.2 nm along the *c*-axis. As a result, the superconducting order parameter is susceptible to structural and chemical changes on atomic length scales. Thus, very small imperfections in the Josephson barrier or at the interface between the barrier and electrodes can drastically affect I_C, since it depends exponentially on the length of the barrier. Therefore, precise control at the nanometer scale is required to make multiple HTS junctions with uniform I_C. HTS Josephson devices are further complicated by anisotropic electrical transport: conductivity along the *c*-axis is 2 orders of magnitude smaller than that in the *a*-*b* plane [21].

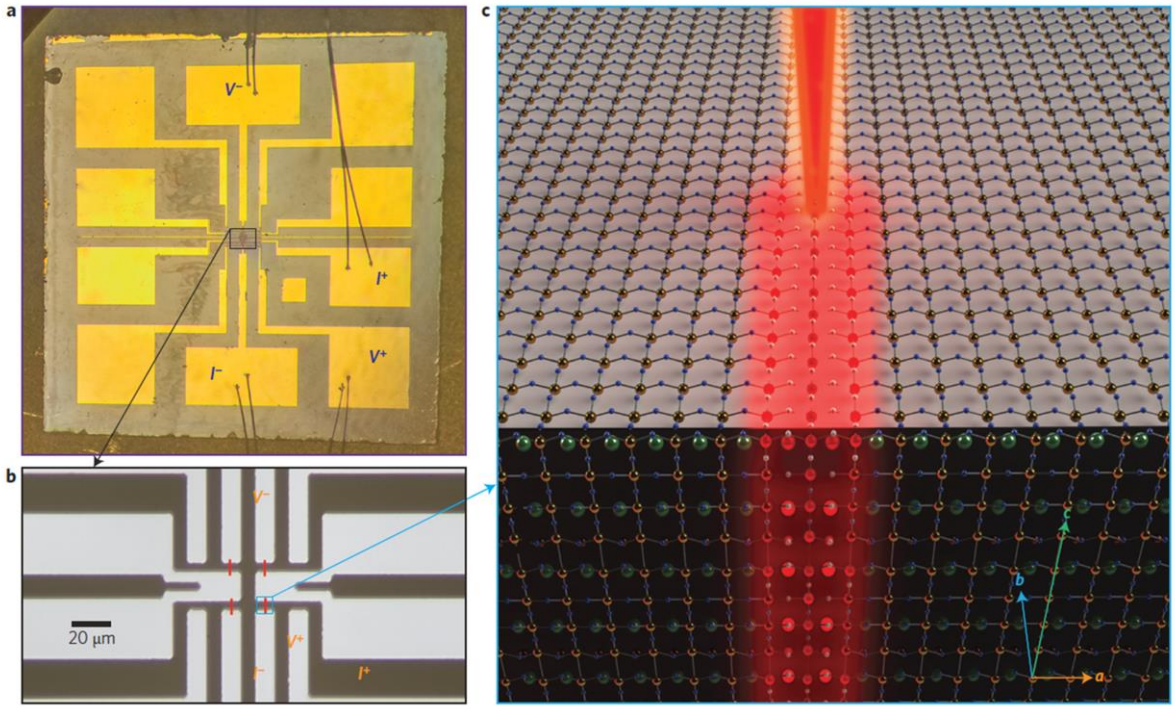

Fig.3: Focused helium ion beam Josephson junction fabrication. (a) Photograph of a photolithographically patterned Au/YBCO film on a 5x5 mm sapphire substrate. (b) View of the central substrate region showing where the gold contact region and YBCO film were etched prior to junction fabrication. This particular pattern contained four, 4-μm wide contacts for four-point resistance measurements. The red lines represent where the helium ion beam was scanned to create the junctions. The current (*I*) and voltage (*V*) leads for one of these bridge is labeled. (c) A schematic of the focused helium ion beam creating a Josephson junction in the YBCO film.

Such anisotropy precludes the possibility of growing epitaxial multilayers to form sandwich type junctions because high quality HTS thin films have *c*-axes orientated normal to the substrate.

Recently, the Cybart group at UCR has developed a new type of HTS Josephson junction [15] employing the use of a finely focused helium beam to directly irradiate the material with no photoresist. The gas field ion source [22] in this machine can be focused as small as 0.5 nm, and create features much smaller than those made with electron beam lithography. The key to this method is that the HTS material is very sensitive to the oxygen order in the crystal lattice which can be altered by light ion irradiation [23]. Large circuit features for electrical contacts and 4-μm wide strips of YBCO were patterned with photolithography in a YBCO thin film that had an *in-situ* deposited Au contact layer on top **(Fig.3a)**. The starting YBCO film thickness was 150 nm, but the Au was removed and the YBCO was etched to a thickness of ~30 nm in the area **(Fig.3b)** intended for junctions to ensure that the 30 kV beam could fully penetrate the film. Samples were then loaded into a Zeiss Orion helium ion microscope and the 30 kV helium beam was scanned across the 4-μm wide superconducting bridges to create the Josephson tunnel barriers **(Fig.3c)**.

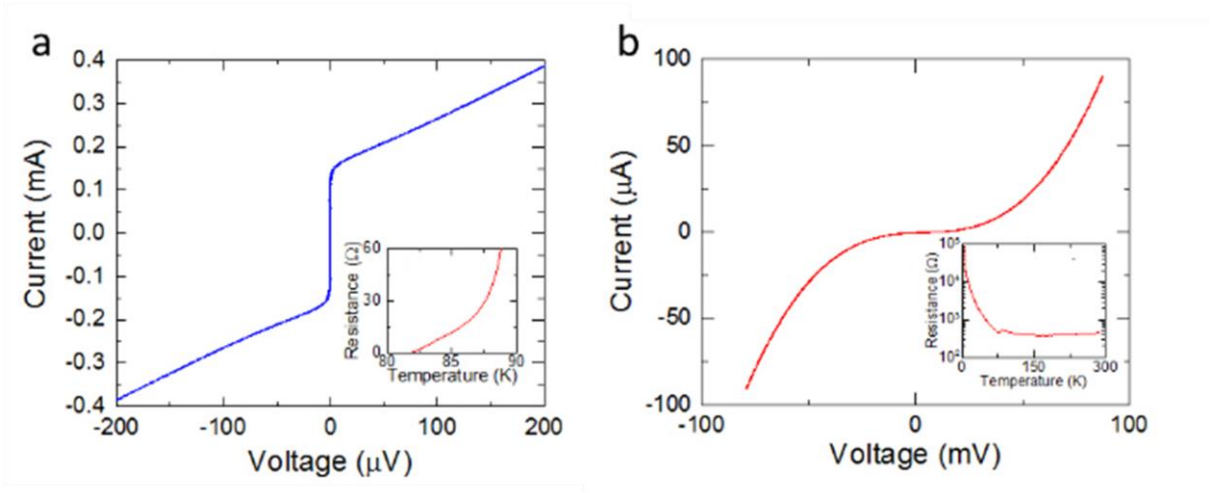

Fig.4: Measurements for YBCO samples irradiated with small (a) and large (b) doses. (a) *I-V* characteristic with large excess current for a dose of 1 × 10^{16} He^{+}/cm^{2}. The inset shows resistance as a function of temperature of the reduced T_C superconductor barrier. (b) Tunnel junction-like *I-V* characteristic for a high dose of 6x10^{17} He^{+}/cm^{2}. The inset shows resistance rapidly increasing as a function of decreasing temperature for the insulating barrier.

Many test samples were written with ion fluence ranging between 10^{14} and 10^{18} He^{+}/cm^{2}. At the lower values very little Josephson current was observed and Andreev reflections (excess current) dominated transport **(Fig.4a)**, similar to what is observed in very broad proximity effect devices [24]. In contrast, at the higher doses the devices exhibited strong localization characteristics with insulating behavior in the barrier **(Fig.4b)**. In between these two extremes we were able to determine doses that could create very high-quality Josephson junctions and continuously transition from superconductor-normal metal-superconductor (SNS) junctions, well described by the resistively shunted junction model (RSJ) [16, 17], to superconductor-insulator-superconductor (SIS) Josephson tunnel junctions.

2.3 SNS and SIS Junctions

The current-voltage characteristics (IVC) are shown in Fig.5**a** for a typical SNS Josephson junction measured at several temperatures. The resistance of ~1 Ω is 10 times larger than masked ion irradiated

weak links [25]. The Fraunhofer diffraction pattern of the supercurrent in applied magnetic field (Fig.5**a** inset) demonstrates the dc Josephson effect, though the pattern is skewed due to self-field effects from the very high current density of 100 kA/cm2 [26]. The temperature dependence of I_C, R_N and their product is shown in Fig.5**b**, and Fig.5**b** inset. The decrease in resistance as temperature is lowered indicates the barrier is a conductor. The temperature range for RSJ characteristics (~30 K) is much larger than that for masked ion irradiated junctions[24] (~3 K) suggesting that the strength of the barrier is much higher and more efficient at suppressing the Andreev reflection transport mechanism.

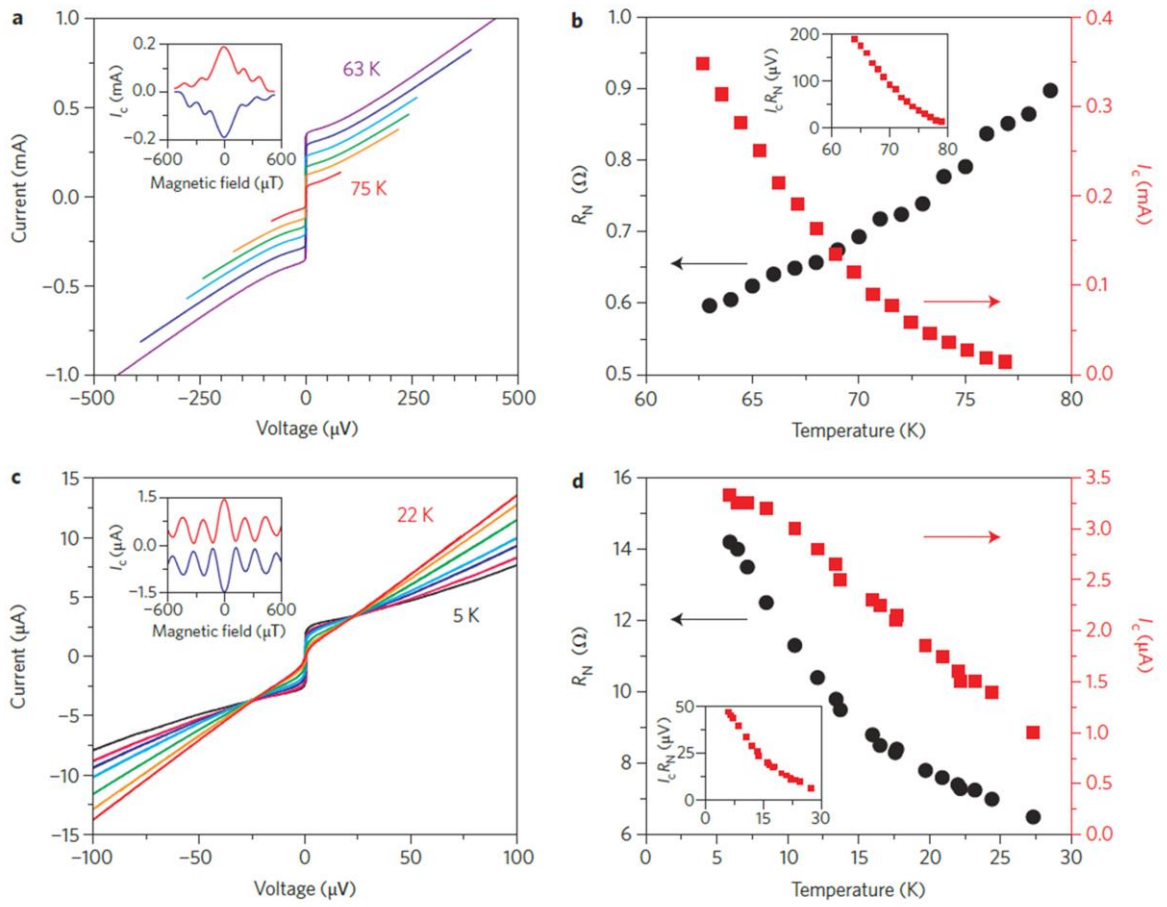

Fig.5: Electrical measurements for a SNS Josephson junction fabricated using a dose of 2 × 1016 He+/cm2. (a) I-V characteristics measured for temperatures 63, 65, 67, 69, 71, and 75 K. (inset) The Fraunhofer diffraction pattern for the critical current in magnetic field. (b) The temperature dependence of the IC, RN and their product. Electrical measurements for a SIS Josephson junction fabricated using a dose of 6 × 1016 He+/cm2. (c) I-V characteristics measured at 5, 10, 12, 14, 16, 18, and 22 K. (inset) The Fraunhofer diffraction pattern for the critical current in magnetic field at 6 K. (d) The temperature dependence of I_C and R_N .

In stark contrast to the SNS junction, Fig.5**c** shows *I-V* for several temperatures of a YBCO, SIS junction fabricated by irradiation with a higher dose (6×10^{16} He^{+}/cm^{2}) . Increasing irradiation levels has the effects of increasing resistivity and reducing the superconducting transition temperature. At modest irradiation levels the material becomes insulating and no longer conducts or superconducts. It is thought that oxygen is being removed and changing the phase of the material to a non-superconducting one, such as $YBa_2Cu_3O_6$. Restricting this converted region to the nanoscale allows for the creation of in-plane quantum tunneling barriers directly in the material with no resists or etching. Because no material is removed or etched, there are no interfaces and the junctions can be made precisely on the nanometer

scale. Furthermore, these junctions do not exhibit hysteresis in the *I-V* characteristic like typical SIS junctions because the Stewart-McCumber parameter [16, 17], $\beta_C = 2\pi R^2 C/\Phi_0$, where R is the normal state resistance, C is the capacitance and Φ_0 is the flux quantum, is very small ($\beta_C \sim 0.001$). This comes about from a small capacitance because of the small area of the planar electrodes normal to the transport direction.

The Fraunhofer diffraction pattern for this junction is shown in (Fig.5**c** inset). The amplitudes of the side lobes fall off much slower than the patterns from ideal sandwich junctions because the current is concentrated closer to the edges. This effect was predicted in work describing the magnetic field characteristics of planar Josephson junctions. Unlike the junction shown in Fig.5**a**, the resistance of this junction increases as temperature is decreased indicating that the barrier is an insulator (Fig.5**d**). Furthermore, unlike the SNS junction, the critical current more weakly depends on temperature and is asymptotic at low temperatures as expected for an insulating barrier junction (Fig.5**d**).

Transport data for the same junction from Fig.5**c** is shown measured at higher current bias in Fig.6. The SIS nature of I-V (Fig.6**b**) is more apparent and conductance peaks are visible at in the derivative (Fig.6**c**) around V = ±32 mV, which we attribute to the gap edge of the superconductor from quasi particle tunneling. This is rarely seen in HTS junctions because it requires a very narrow <3 nm insulating barrier. This observance is a testament to the quality and potential of helium ion direct-write lithography to pattern sub-10nm features.

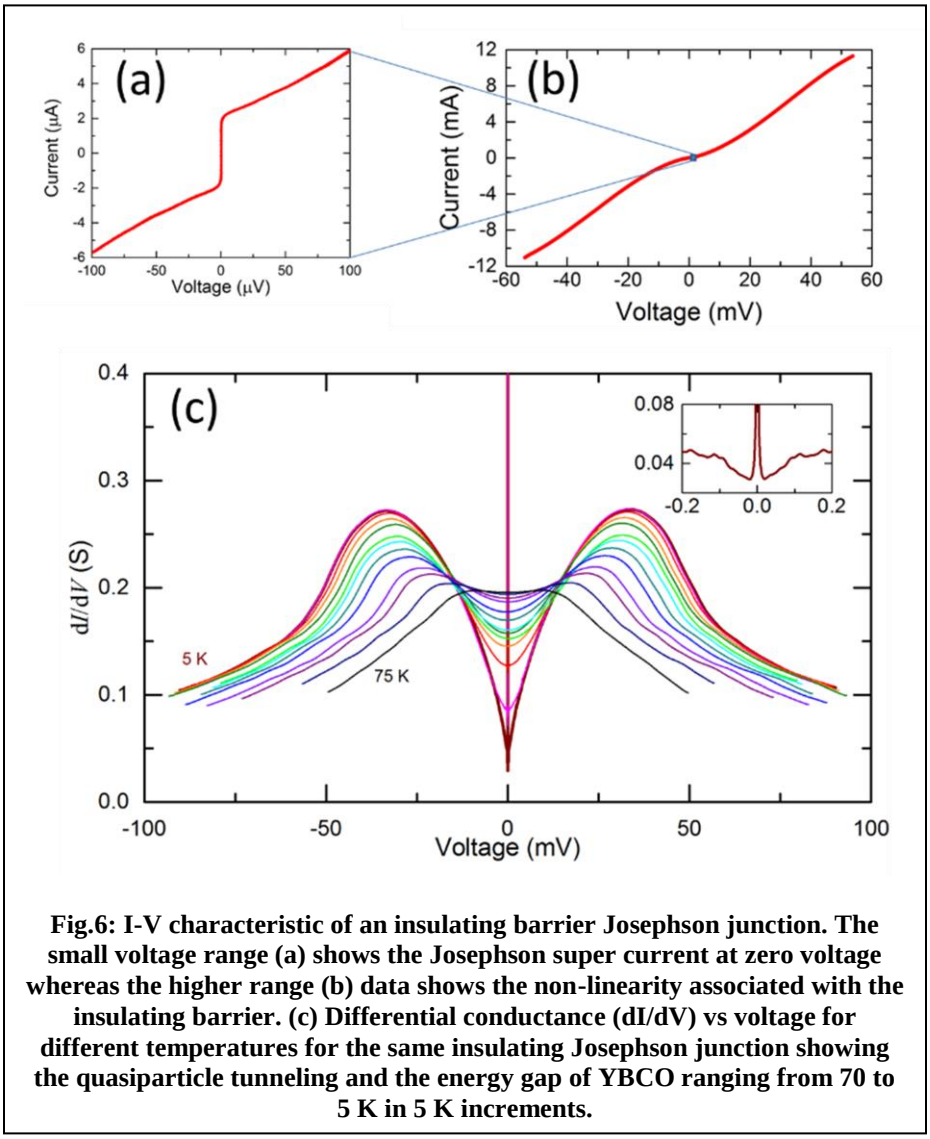

Fig.6: I-V characteristic of an insulating barrier Josephson junction. The small voltage range (a) shows the Josephson super current at zero voltage whereas the higher range (b) data shows the non-linearity associated with the insulating barrier. (c) Differential conductance (dI/dV) vs voltage for different temperatures for the same insulating Josephson junction showing the quasiparticle tunneling and the energy gap of YBCO ranging from 70 to 5 K in 5 K increments.

This work demonstrated a new level of control that can be achieved in HTS junction fabrication. To illustrate this we present electrical transport data for Josephson junctions written with different irradiation doses ranging from 75 to 375 ions/nm in Fig.7. From this data it can be seen that the junction crossover from metal to insulator near a dosage at 200 ions/nm. This is significant for electronics because resistively shunted junctions can exhibit excess

current, which is independent of the Josephson equations. Furthermore for this particular material and geometry we observed $I_C R_N$ products close to 1mV which are approximately ten times higher than most HTS devices.

These junctions have several desirable features which make them good candidates for THz electronics. As mentioned previously they can be made with small excess currents and high $I_C R_N$ products. Fig.8 is an example of a high $I_C R_N$ junction fabricated using the helium ion direct write approach. We expect devices of this quality to operate up to approximately 3 THz.

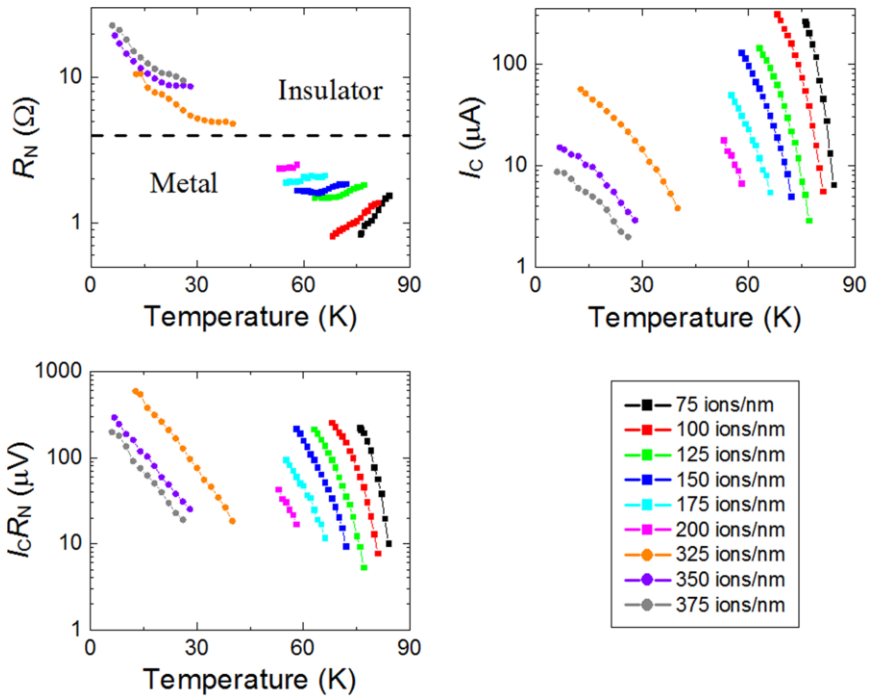

Fig.8: Metal-insulator transition of the normal state resistance of YBCO Josephson junctions written for a range of irradiation doses. At the highest doses R_N is increasing with lower temperature as expected for an insulator whereas at lower doses the behavior is that of a metal (decreasing R with lower temperature).

These devices are the first insulating barriers created in all YBCO junctions in a reproducible manner. While the barriers are not as strong as those in conventional niobium circuits, they are nonetheless an order of magnitude better than prior ion irradiated devices. The ease of the process and the relatively few numbers of processing steps opens up a promising pathway to a new large scale inexpensive manufacturing process that can deliver HTS circuits for myriad applications.

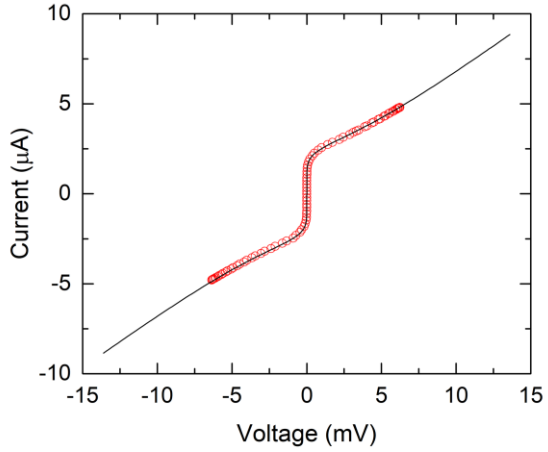

Fig.7: I(V) for a junction with $I_C R_N$ approximately 5mV. The black line is a fit to the data.

3.0 RESULTS AND DISCUSSION

3.1 Emitter Design and Fabrication

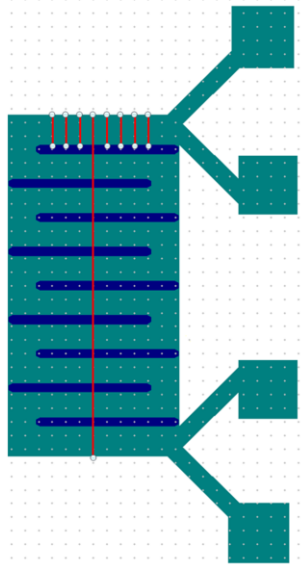

Figure 9: Meander Array design.

The first step of this Phase I effort was to design the THz source emitter. Our initial resonator design concept employed the use of a meander path to maximize the number of junctions in the series array. However, based on the index of refraction of YBCO (probably similar to that of BSSCO), inter-junction spacing would need to be on a length scale of nanometers to reach THz frequencies. Based on our approach of using a helium ion microscope to perform the junction nano-lithography, we can achieve a junction width of <2 nm, and can probably reach inter-junction spacings of better than 10 nm, so this approach was considered. For the ensuing simulation studies, our input parameters were that the junctions would be so-called long junctions, with electrode widths between 12 and 25 µm. The 30 to 50 nm thick YBCO films are not de-twinned, and we estimated an $I_C R_N$ product of ~ 400 µV for each junction in the array. We sought to investigate simulated transmitter response for 10, 100, and 1000 junctions, look at how inter-junction spacing affects the output frequency, and investigate polarization and directionality of radiated power. **Figure 11** illustrates our meander array design, with the junction locations shown in red. The blue lines indicate where the meander pattern is to be defined using helium ion beam nano-lithography.

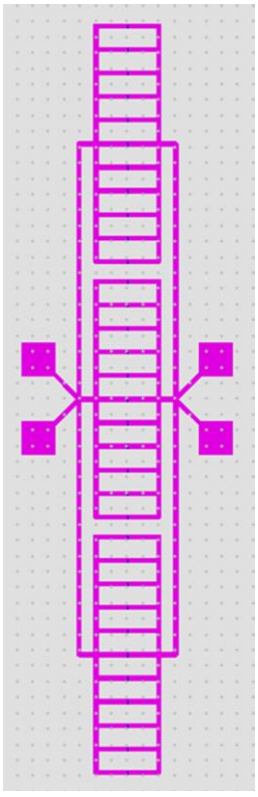

Figure 10: Ladder Array design.

Since the Josephson current oscillates in the direction of DC current flow across the junction, and the polarization of the associated emitted radiation is in the direction of the electric field across the junction, each junction may be considered as an electric dipole. However, after careful thought, calculation, and simulation, it is clear that the spatially-alternating path that the current takes would generate electromagnetic (EM) waves of alternating polarities out of the junctions, and would likely result in destructive interference. The polarization and directionality results of the simulation eliminated the meander array as a candidate emitter design.

We then investigated the possibility of arranging the electrodes containing the Josephson junctions in parallel, both so that the directions of the Josephson currents are consistent and that the applied voltage across each junction is the same. This approach will generate electromagnetic waves from each junction with identical polarizations and matching frequencies. We designed the junction array in the fashion of a "ladder", with each "rung" containing the location(s) of the junctions, as shown in **Figure 10**. With an inter-rung spacing of 8 µm, such a pattern could be nano-fabricated using only three focal write fields of view of the helium ion microscope, a 100 µm by 100 µm area. To increase the radiated power, we also have the option of patterning high-density Josephson arrays in each parallel electrode, as the radiated power is purported to scale with the square of the number of junctions in series.

However, since our ultimate goal was to employ a separate Josephson device to measure the emitted radiation, we had to consider the issue of optimal positioning of the detector with respect to the emitter, and the subsequent complication of making electrical interconnection to the electrodes of each device. Since the directionality of the THz radiation

pattern from each junction in the array can be modeled as an electric dipole, the primary lobe will be normal to the substrate due to constructive interference from the ensemble of junctions. Since the optimal location of the detector was therefore directly above the center of the emitter array, the interconnection of the electrodes had to be realized at the edge of the device chip. Furthermore, this required the center of the emitter array to be laterally offset from the center of the 5 mm by 5mm sample, and that the receiver positioned above the staggered center of the emitter, exposing the bond pads of the emitter device for wire bonding access. The re-designed parallel emitter device is shown in **Figure 11**., with the As an added manufacturing benefit, this array design fits within two fields of view of the helium ion microscope.

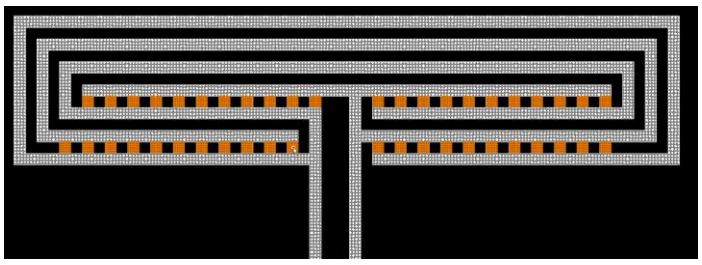

Figure 11: Circuit layout of resonator design, with the location of the junction arrays highlighted

Assuming a conservative inter-junction spacing of 200 nm for each array, each 4 µm long electrode can contain up to 20 junctions. With 44 of these junction arrays in parallel, this could give a total of 880 junctions in the device.

Figure 12: Bowtie Antenna design. Josephson junction gets patterned where the points intersect.

3.2 Receiver Design

For the THz detector, we patterned a single Josephson junction at the point contact of a standard bowtie antenna, in order to maximize the bandwidth of detection. Since the transmitter and detector are both patterned on 5 x 5 mm chips, the transmitter array is shifted off-center by 1 mm in the design. This allows for the detector to be positioned directly above the transmitter, while allowing 1 mm of wire bonding access to the underneath chip. **Figure 12** illustrates the bowtie antenna / Josephson detector design.

3.3 Receiver Testing

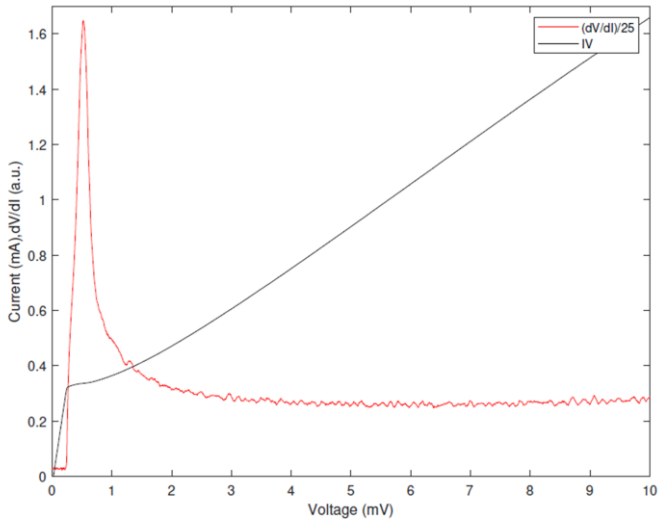

Figure 13: Differential resistance measurement of single nano-junction.

As a proof of concept, we have also performed measurements of a single nano-junction, patterned into a spiral antenna, when irradiated with varying levels of microwave power from a very high-frequency source (0.6 THz). The measurements were performed by superimposing an AC bias current (~1 kHz) on top of the dc bias current. The differential resistance was measured by phase-sensitive detection of the ac voltage response while the device was subjected to 0.6 THz microwave radiation. **Figure 13** plots the current-voltage characteristic (IVC) and the differential resistance (dV/dI) of a single junction without being subjected to microwave radiation. The peak in differential resistance is observed at the critical current transition, as expected.

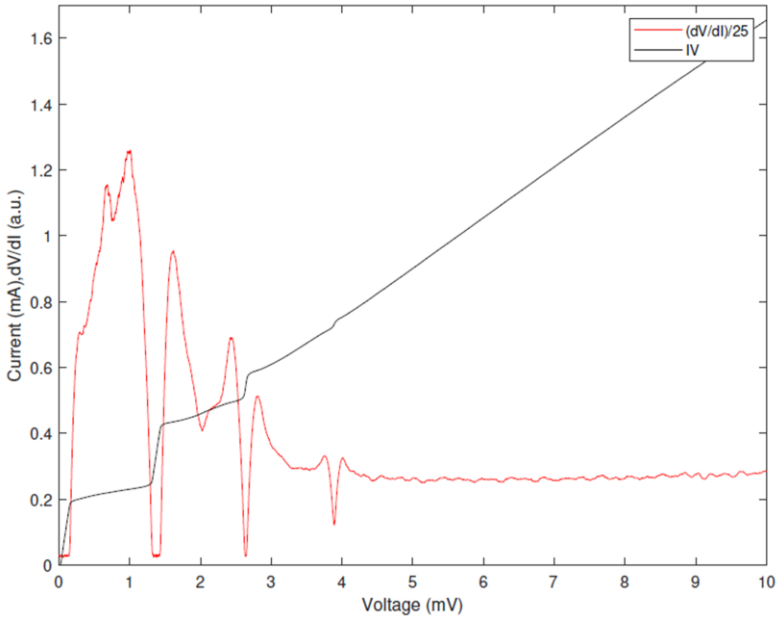

Figure 14: Current-Voltage characteristic of single nano-junction at low 600 GHz power.

Figure 14 is a plot of the IVC and dV/dI of the same junction when irradiated with a low-power level from the 0.6 THz source. The local minima in the differential resistance reveal 3 orders of Shapiro steps, located at the Josephson voltages equal to the harmonics of the frequency of applied THz radiation.

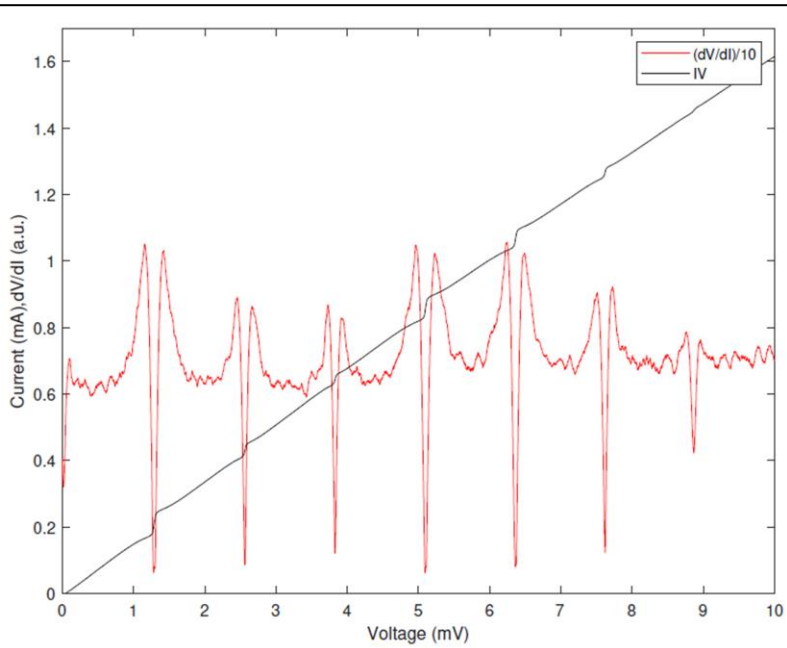

Figure 15: IVC and dV/dI at higher microwave power.

Figure 15 displays the IVC and dV/dI of the junction when irradiated with a higher power level from the 0.6 THz source. Shapiro steps are evident out to the 7th order, at roughly 9 mV, suggesting that this method will allow us detection capabilities out to greater than 4 THz using this approach.

3.4 Coupled Emitter/Receiver Testing

The emitter and receiver designs were sent to SQUIDWorks, LLC, for fabrication. The first batch yielded an operational emitter and receiver, albeit at greatly different optimal operating temperatures between them (**Figure 16**). Subsequently, the emitter became open-circuited after its 1st thermal cycling, so the first attempt at testing these devices together had to be halted.

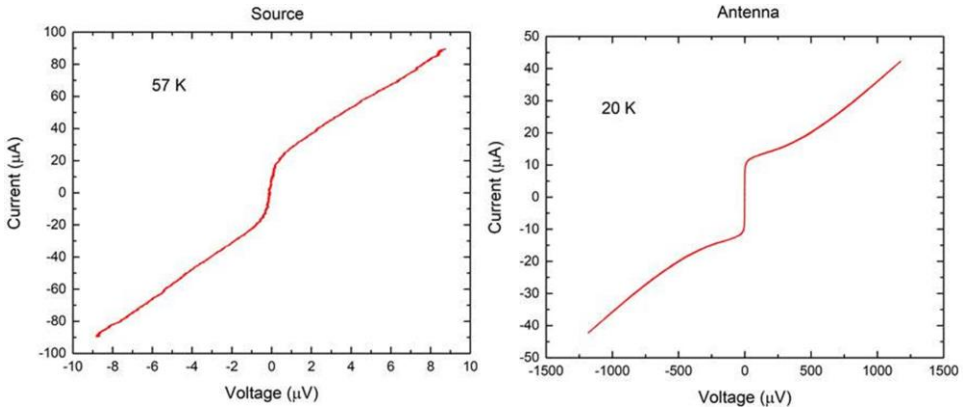

Figure 17: I-V Characteristics of the initial source and antenna samples

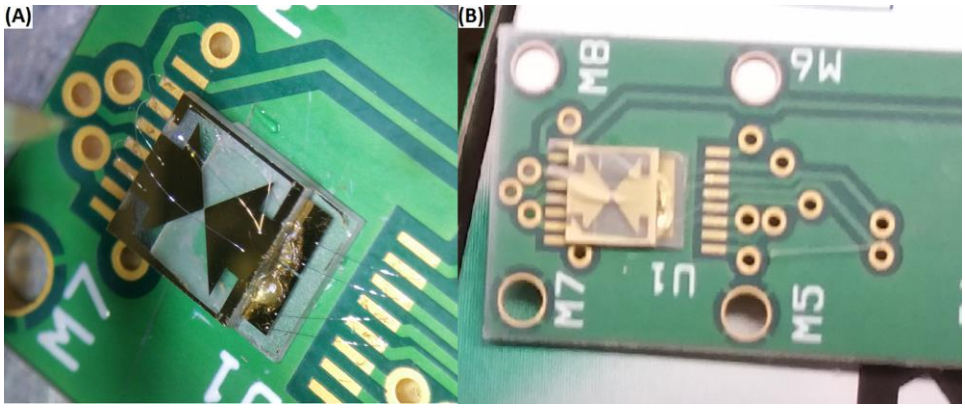

Figure 16: (a) 2nd Emitter and Receiver samples wire bonded to PCB, and (b) after thermal cycling.

A second run provided more promising results. The devices were aligned and wire bonded to an interconnection board (**Figure 17(a)**), which was then mated to cryogenic cabling in the cryogenic test probe. We successfully used silicone high-vacuum grease to adhere the samples together, as they were still accurately aligned when removed from the cryogenic environment (**Figure 17(b)**).

The emitter and receiver were tested in tandem for their IVCs and for any potential coupling. **Figure 18(a)** shows the large I_C of the emitter at 10 mA and an apparent R_N of 0.4Ω. **Figure 18(b)** displays a more functional I_C of the receiver of 135 μA and an R_N of 17 Ω.

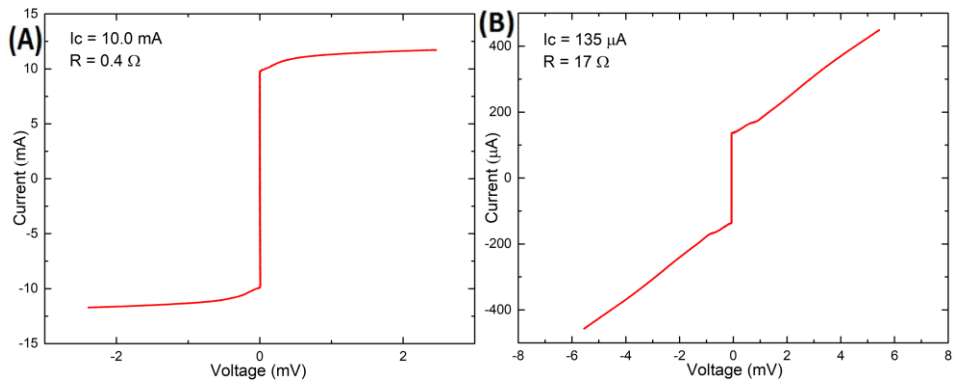

Figure 18: I-V characteristics of (a) emitter and (b) receiver at 4 K.

The emitter and detector were biased at orthogonal frequencies, decades apart. The penultimate measurement was a 10 Hz I-V sweep of the detector acquired at 50 kiloSamples/second with a one second acquisition time, granting a 10-fold stacking average. Meanwhile, the emitter was swept at 0.01 Hz. We were hoping to observe a slowly-moving Shapiro step in the IVC of the detector, co-located at the quasi-static voltage applied across the emitter junctions at that point in time of the 0.01 Hz sweep.

Unfortunately, no Shapiro steps were observed. There are a few culprits as to why this was the case. First and foremost, only one junction per parallel rung in the emitter array was patterned, instead of the Phase I design goal of 20 and Phase II design goal of 200. Since the radiated power is proportional to $\sim N^2$, it is entirely possible that not enough power was being radiated to reach the threshold of detection. It is also possible, due to parameter spread in the 44 parallel junction array, that I_C was much lower in a few junctions. Thus, they would be carrying the entire current load instead of having all the junctions in the array work together in concert. Yet another possibility is that the extremely high I_C of 10 mA is actually the critical current of the film itself at 4K, as suggested by the extreme change in the IVC slope when I_C is exceeded. However, a significant probability is that the radiated emissions were suppressed due to parasitic interaction with the substrate, necessitating the simulation studies on substrate interaction in the following section.

3.5 THz Simulation

The prior cryogenic tandem test results, or lack thereof, motivated the simulation study of radiation lobe pattern as a function of substrate dimensions and frequency for a given junction array pattern. As we had anticipated this interaction, our simulation results are included below.

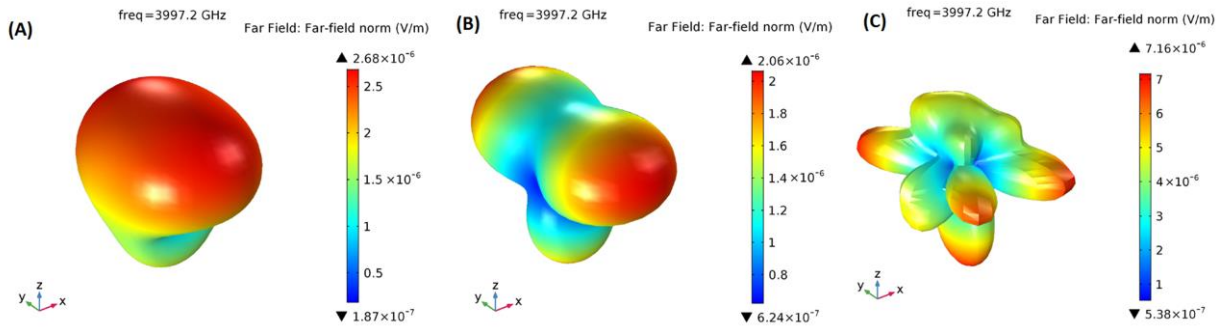

Figure 19: Electric field radiation patters of a 17-juunction meander array at 4 THz for substrate dimensions (L x W x H) of (a) 20 µm square by25 µm thick, (b) 20 µm square by35 µm thick, and (c) 75 µm square by50 µm thick.

In **Figure 19**, the calculated dependency of the electric field upon substrate dimensions is displayed. The radiation pattern from a meander path of three parallel lines including 17 Josephson junctions was simulated at 4 THz for substrates of varying dimensions, from a 20 µm square by 25 µm thick (**Figure 19(a)**), to a thicker (35 µm) substrate (**Figure 19(b)**), up to a 75 µm square by 50 µm thick substrate (**Figure 19(c)**). The substrate acts as a parallel inductive-resistive-capacitive (LRC) resonant cavity. When the substrate dimensions are increased, the resonant frequency of the cavity formed by the substrate decreases. The effect of the substrate dimensions is especially troubling when one considers that our nominal substrate dimensions are a 5000 µm square by 500 µm thick, meaning that we will need to address this issue in Phase II.

This parasitic substrate resonance effect was also simulated with a fixed size of a 75 µm square by 50 µm thick while varying the frequency from 0.2 THz to 6.0 THz. The simulated electric field radiation patterns are shown in **Figure 20**. Again, when one considers that our nominal substrate dimensions are

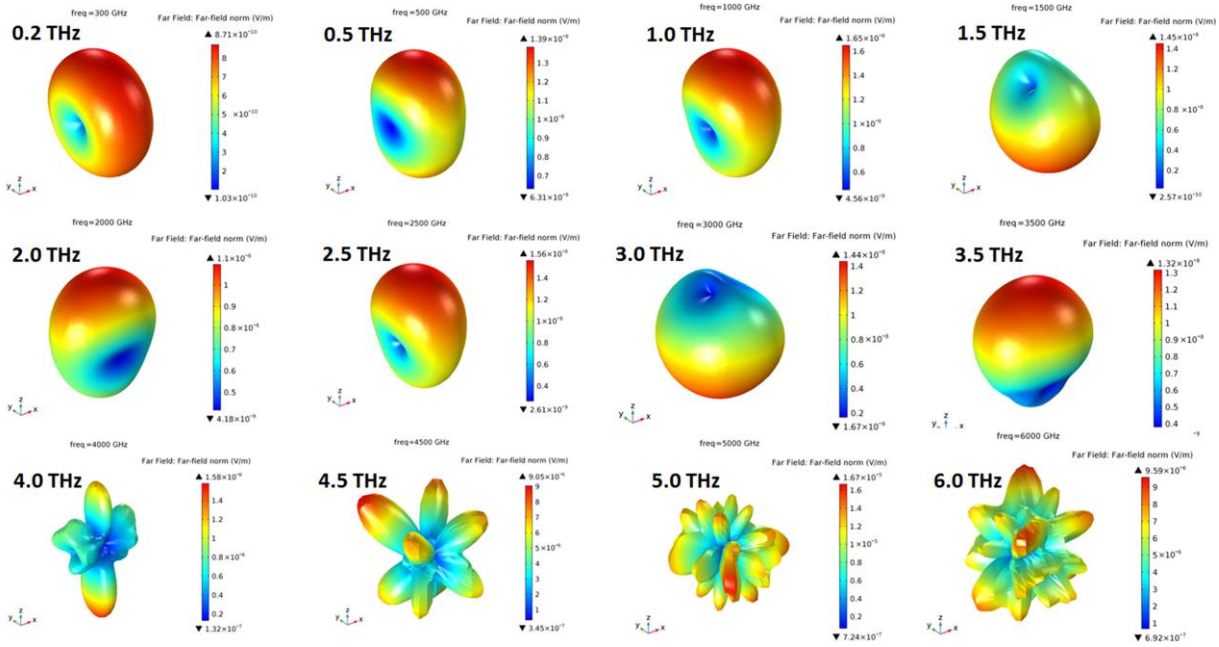

Figure 20: Electric field radiation patters of a 17-juunction meander array substrate dimensions (L x W x H) of a 75 µm square by50 µm thick for frequencies ranging from 0.2 THz to 6.0 THz.

more than 4000 times larger in area and 10 times thicker, it is evident that this parasitic loading of the emitter by the substrate will have to be addressed in Phase II. Our plan is to pattern the emitter and receiver on multi-layer substrates, so that the buried layer of YBCO will act as a reflective ground plane in an attempt to mitigate the unwanted influence of the substrate.

3.6 Cryopackage Design

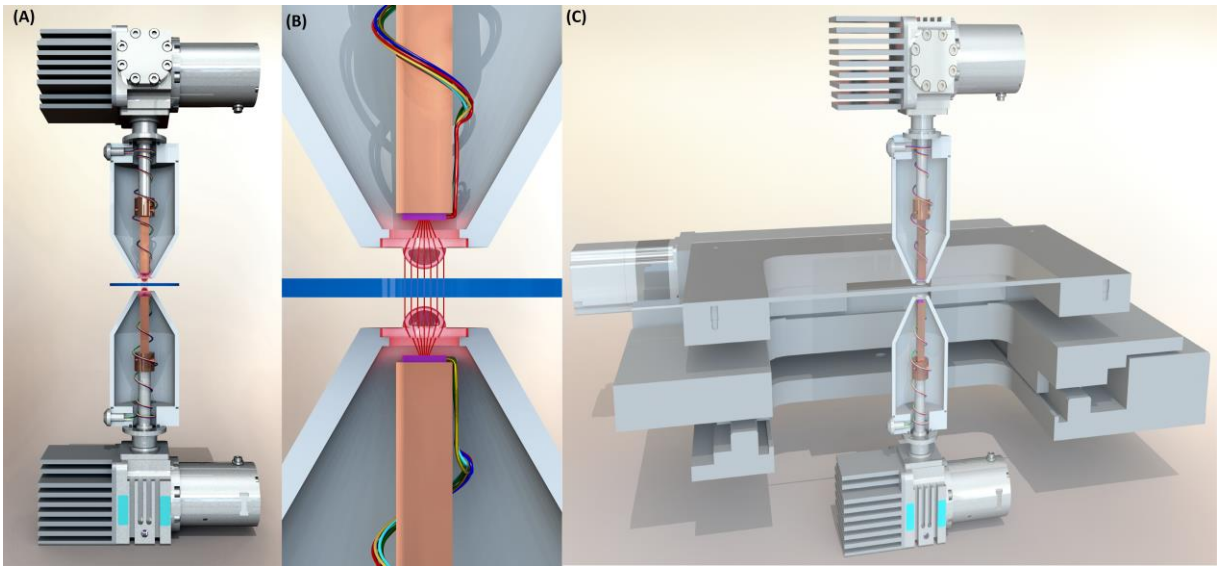

Figure 21: Cryopackaging of Phase II prototype THz spectrometer.

In this Phase I effort, we were also tasked with developing a cryopackaging design for a Phase II prototype. Our concept is that of a THz spectrometer employing dual cryogenic transmitter/receiver packages positioned on opposite sides of the sample-under-test (**Figure 21(a)**). Hemispherical lenses ground from silicon will be used to collimate and focus the beam(s). Each dewar is cooled by a commercial Stirling cycle cryocooler.

The sample is interrogated at orthogonal frequencies by the two transmitters, and each of the two receivers is continuously AC biased to search for Shapiro steps corresponding to the voltage applied to the transmitter in its own dewar and the transmitter in the opposite dewar (**Figure 21(b)**). This allows for the measurement of both reflection and transmission spectra of the sample, enabling the calculation of the absorption spectrum.

Furthermore, the prototype spectrometer can be equipped with a scanning stage with micron resolution to permit non-destructive evaluation of a sample at THz frequencies (**Figure 21(c)**).

The employment of Commercial-Off-The-Shelf (COTS) single-stage Stirling-cycle cryocoolers will be beneficial to this project by simplifying the cryogenic requirements of the system. These devices typically have a cryocooler lift of ~ 1 Watt at 77 Kelvin and require nominally 40 to 50 Watts of electrical power for their operation. This removes the requirement of cryogenic handling and safety from the operator perspective. Cryocoolers of this type typically have minimum temperatures approaching 40 Kelvin. If the heat load to the cryocooler is properly managed, these machines have the capability of reducing the temperature of the Josephson devices to where the superconducting energy gap is nearly maximized.

4.0 CONCLUSIONS

In this Phase I effort, we studied various Josephson junction array topologies with the goal of designing an optimal compact transmitter at THz frequencies. These array designs were calculated and simulated, and subsequently designed and fabricated. We also investigated receiver geometries that employ single or multiple Josephson junction detectors. Wideband receivers employing Josephson junction detectors were also designed and fabricated, and subsequently tested for their ability to detect radiation in the THz regime. These transmitter and receiver devices were then tested in tandem with the goal of using the receiver to detect power radiated from the emitter at THz frequencies. Though this aspect of the test was unsuccessful, we have multiple paths forward to optimize the devices in Phase II. Furthermore, we have developed a cryopackaging solution for a Phase II prototype THz spectrometer employing these HTS THz transmitters and receivers to interrogate the transmission, reflection, and absorption spectra of a sample-under-test.

5.0 REFERENCES

1. A. K. Jain, P. Mankiewich, and J. E. Lukens, "Observation of Phase Coherence among Multiple Josephson Oscillators," *Applied Physics Letters*, vol. 36, pp. 774-776, 1980.
2. A. K. Jain, P. M. Mankiewich, A. M. Kadin, R. H. Ono, and J. E. Lukens, "Microwave Wideband Tunable Oscillators Using Coherent Arrays of Josephson-Junctions," *Ieee Transactions on Magnetics*, vol. 17, pp. 99-102, 1981.
3. J. E. Sauvageau, A. K. Jain, and J. E. Lukens, "Millimeter-Wave Phase-Locking in Distributed Josephson Arrays," *International Journal of Infrared and Millimeter Waves*, vol. 8, pp. 1281-1286, Oct 1987.
4. J. E. Sauvageau, A. K. Jain, J. E. Lukens, and R. H. Ono, "Phase-Locking in Distributed Arrays of Josephson Oscillators," *Ieee Transactions on Magnetics*, vol. 23, pp. 1048-1050, Mar 1987.
5. K. Wan, A. K. Jain, and J. E. Lukens, "Submillimeter Wave Generation Using Josephson Junction Arrays," *Applied Physics Letters*, vol. 54, pp. 1805-1807, May 1 1989.
6. B. K. Bi, K. Wan, W. X. Zhang, S. Y. Han, and J. E. Lukens, "Josephson-Junction Driven Submillimeter Wave Microstrip Resonator," *Ieee Transactions on Applied Superconductivity*, vol. 1, pp. 145-149, Dec 1991.
7. K. Wan, A. K. Jain, L. A. Fetter, W. Zhang, S. Han, and J. E. Lukens, "Development of a Rapidly Tunable Microwave Source," *Superconductor Science & Technology*, vol. 4, pp. 647-649, Nov 1991.
8. K. Wan, B. Bi, A. K. Jain, L. A. Fetter, S. Han, W. H. Mallison, *et al.*, "Refractory Submillimeter Josephson Effect Sources," *Ieee Transactions on Magnetics*, vol. 27, pp. 3339-3342, Mar 1991.
9. B. K. Bi, S. Han, and J. E. Lukens, "Radiation Linewidth of Phase-Locked Distributed Array in the Submillimeter-Wave Range," *Applied Physics Letters*, vol. 62, pp. 2745-2747, May 31 1993.
10. B. K. Bi, S. Han, J. E. Lukens, and K. Wan, "Distributed Josephson Junction Arrays as Local Oscillators," *Ieee Transactions on Applied Superconductivity*, vol. 3, pp. 2303-2306, Mar 1993.
11. S. Y. Han, A. H. Worsham, and J. E. Lukens, "Complete Phaselocking in a One-Dimensional Series Biased Josephson-Junction Array," *Ieee Transactions on Applied Superconductivity*, vol. 3, pp. 2489-2492, Mar 1993.
12. M. K. Wu, J. R. Ashburn, C. J. Torng, P. H. Hor, R. L. Meng, L. Gao, Z. J. Huang, Y. Q. Wang, C. W. Chu; "Superconductivity at 93-K in a New Mixed-Phase Y-Ba-Cu-O Compound System at Ambient Pressure", *Phys Rev Lett*, **58**, 1987.
13. D.Y. An *et al*; "Terahertz emission and detection both based on high-Tc superconductors: Towards and integrated receiver", *Applied Physics Letters*, **102**, 2013.
14. R.A. Klemm, E.R. LaBerge, D.R. Morley, T. Kashigawi, M. Tsujimoto, and K. Kadowaki; "Cavity mode waves during terahertz radiation from rectangular $Bi_2Sr_2CaCu_2O_{8+\delta}$ mesas", *J. Phys.: Cond. Matter*, **23**, 2011.
15. S. A. Cybart, E. Y. Cho, T. J. Wong, B. H. Wehlin, M. K. Ma, C. Huynh, and R. C. Dynes; "Nano Josephson superconducting tunnel junctions in $YBa_2Cu_3O_{7-\delta}$ directly patterned with a focused helium ion beam", *Nature nanotechnology* **10**, 2015.
16. B. D. Josephson; "Possible New Effects in Superconductive Tunnelling", *Physics Letters*, **1**, 1962.
17. W. C. Stewart; "Current-Voltage Characteristics of Josephson Junctions", *Appl. Phys, Lett.*, **12**, 1968.
18. D. E. McCumber; "Effect of AC Impedance on DC Voltage-Current Characteristics of Superconductor Weak-Link Junctions", *J Appl. Phys.*, **39**, 1968.
19. D. Koelle, R. Kleiner, F. Ludwig, E. Dantsker, J. Clarke; "High-transition-temperature superconducting quantum interference devices", *Rev Mod Phys*, **71**, 1999.
20. J. T. Kim, J. Giapintzakis, D. M. Ginsberg; "Anisotropy of the resistivity in the a-b plane of a superconducting $YBa_2Cu_3O_{7-\delta}$ single crystal", *J Supercond*, **9**, 1996.

21. A. Samsavar, T. Miller, T. C. Chiang, B. G. Pazol, T. A. Friedmann, and D. M. Ginsberg; *Phys Rev B*, **37**, 1988.
22. B. Ward, J. A. Notte, and N. P. Economou, "Helium-ion microscopy," *Photonics Spectra*, vol. 41, pp. 68-70, Aug 2007.
23. A. E. White, K. T. Short, R. C. Dynes, A. F. J. Levi, M. Anzlowar, K. W. Baldwin, P. A. Polakos, T. A. Fulton, and L. N. Dunkleberger; "Controllable Reduction of Critical Currents in $YBa_2Cu_3O_{7-\delta}$ Films", *Appl Phys Lett*, **53**, 1988.
24. K. K. Likharev, "Superconducting Weak Links," *Reviews of Modern Physics*, **51**, pp. 101-159, 1979.
25. S. A. Cybart, S. M. Anton, S. M. Wu, J. Clarke, and R. C. Dynes, "Very Large Scale Integration of Nanopatterned YBa2Cu3O7-delta Josephson Junctions in a Two-Dimensional Array," *Nano Letters*, **9**, pp. 3581-3585, Oct 2009.
26. Owen, C.S. and Scalapino, D.J., *Vortex Structure and Critical Currents in Josephson Junctions.* Physical Review, **164**(2), 1967.

6.0 GLOSSARY OF ACRONYMS

AC – Alternating Current
BSCCO - $Bi_2Sr_2CaCu_2O_{8+\delta}$
BWO – Backward Wave Oscillator
COTS – Commercial-Off-The-Shelf
DC – Direct Current
EM - Electromagnetic
FEL – Free Electron Laser
HTS – High transition-Temperature Superconductor
I_C – Critical Current
IJJ – Intrinsic Josephson Junction
IVC – Current-Voltage Characteristic
JJ – Josephson Junction
LRC – Inductive-Resistive-Capacitive
LTS – Low transition-Temperature Superconductor
NIST – National Institute of Standards and Technology
QCL – Quantum Cascade Laser
R_N – Normal Resistance
RSJ - Resistively-Shunted Junction
SIS – Superconducting-Insulating-Superconducting
SNS – Superconducting-Normally conducting-Superconducting
T_C – superconducting Transition (Critical) temperature
THz – TeraHertz
UCR – University of California, Riverside
YBCO - $YBa_2Cu_3O_7$